Journal of
Materials Chemistry A

Accepted Manuscript

Journal of Materials Chemistry A RSCPublishing

ARTICLE

A SiO_x/C@RGO three dimensional nanocomposite as a high energy anode material for lithium-ion batteries †

Cite this: DOI: 10.1039/xoxxooooox

Chenfeng Guo, Dianlong Wang*, Tiefeng Liu, Bo Wang, Junsheng Zhu and Xiaoshi Lang

Received ooth January 2012,
Accepted ooth January 2012

DOI: 10.1039/xoxxooooox

www.rsc.org/

A co-modification strategy to improve the electrode performance of SiO-based material through the use of carbon coating layer and reduced graphene oxide (RGO) network has been developed. The as-synthesized SiO_x/C@RGO nanocomposites showed excellent specific capacity, cycling performance and rate capability when used as an anode in lithium-ion batteries.

Introduction

Lithium-ion batteries (LIBs) are now considered as the predominant power source for portable electric devices, electric vehicles (EV) and hybrid-electric vehicles (HEV) owing to its low cost, safety, superior stability and high energy density.[1, 2] Graphite is the commercial anode material for LIBs with a limited theoretical capacity of 372 mAh g^{-1}, which still lies behind the demands of consumers. Silicon monoxide (SiO) has been proposed as one of most promising anode candidates for next-generation LIBs, owing to its theoretical capacity was reported to be over 1400 mAh g^{-1} in several papers,[3-5] and low charge-discharge potential. Unfortunately, it suffers from the major problem of poor capacity retention, which prevents SiO from being used in large commercial applications. The intrinsically low electric conductivity (6.7×10^{-4} S cm^{-1}) of SiO[6, 7] and drastic volume changes particles (close to 200% of the initial volume)[8] during Li^+ insertion/extraction process causes cracking and pulverization, which will result in electrical disconnection of active material with current collector and consequently limit the cycling capability of electrodes. Considerable trials have been devoted to coping up this problem such as doping the host framework with guest ions,[9, 10] adding/coating with buffer materials (such as carbon or other conductive materials),[11-14] the methods of chemical and physical pre-reaction,[15, 16] optimizing the morphology,[17] decreasing dimensional size,[11, 13] changing to more effective binders.[18, 19] Among various endeavors, the electrochemical properties of SiO anode can be considerably improved using carbon shells to coat on SiO nanoparticles (NPs). On one hand, the coated carbon layer can effectively retard the growth of Silicon (Si) crystal, which will favor Li^+ insertion/extraction due to the shortened distance for Li^+ diffusion and increased contact area with the electrolyte. On the other hand, the dispersed carbon particles provide pathways for electron transfer and decrease the polarization resistance of the electrode, thus result in the improved conductivity and electrochemical properties. Nonetheless, current carbon-coating technologies still exhibited capacity fading because of the unavoidable agglomeration of small NPs. Therefore, finding a more efficient composite technology to coating carbon with an even more effective carbon source is still a great challenge.

Graphene, a single-atom-thick sheet of honeycomb carbon lattice, exhibits a number of intriguing unique properties,[20-22] such as outstanding electronic conductivity, high surface area, large surface-to-volume ratio and amazing mechanical properties. These properties make graphene or graphene-based materials very promising for use as anode materials for reversible lithium storage in LIBs.[23-28] In LIBs, graphene can be exploited by integrating it as a structural buffer in the anode that can withstand the enormous strains generated during charge/discharge process. However, it is well known that the volume expansion rates of SiO and graphene during Li^+ insertion/deinsertion are significantly different, so it can be imagined that the SiO NPs may peel off from the graphene after several charge/discharge cycles, which was evidenced by the capacity fading of SiO/graphene anode in previous report.[29] In order to avoid detachment of the pulverized SiO NPs, a novel and facial strategy for constructing a three dimensional (3D) composite (denoted as SiO_x/C@RGO) by anchoring SiO_x ($x\approx1$) NPs wrapped within carbon shells onto reduced graphene oxide (RGO) network might be helpful. In this strategy, the carbon shell can act as a buffer that minimizes volume changes and direct contacts between SiO_x NPs and electrolyte, facilitating the formation of a stable solid electrolyte interphase (SEI) film which leads to outstanding cycling performance. Meanwhile, carbon shell is regarded as a conducting bridge between SiO_x NPs and RGO in the nanocomposites (NCPs), the carbon coating layer and RGO network work together to effectively maintain the stability of the structural arrangement, serve as good electron conductors, and allows Li^+ access.[30, 31] However, to the best of our knowledge, there were fewer reports on the SiO_x/C@RGO NCPs as an anode material for LIBs so far. Herein, a novel SiO_x NCPs co-modified by carbon coating layer and RGO network was synthesized. The SiO_x/C@RGO NCPs showed superior specific capacity, cycling performance, and rate capability as compared with only carbon-coated SiO_x sample (designated as SiO_x/C), which was prepared using the sample method of SiO_x/C@RGO except for the presence of RGO.

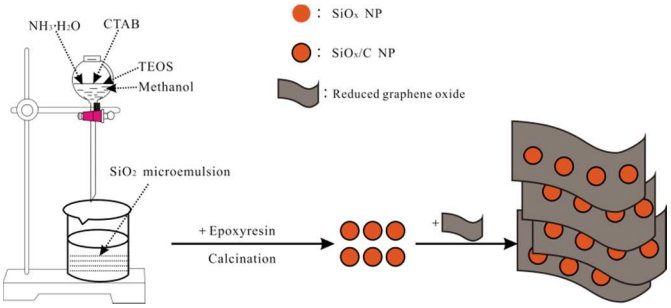

Scheme. 1 Schematic illustration of the formation process of the SiO_x/C@RGO NCPs.

Experiment

Synthesis of SiO_x/C@RGO NCPs

Scheme. 1 illustrates the synthesis procedure for the SiO_x/C@RGO NCPs. The precursor of silica (SiO_2) microemulsion were prepared by a simple one-step procedure route at room temperature, modifying a procedure reported by Robert I. Nooney[32] for the synthesis of spherical mesoporous SiO_2 nanostructures. In a typical synthesis procedure, hexadecyltrimethylammonium bromide (CTAB) (211 mg), deionized water (17.7 g), methanol (175 ml), and 28% aqueous ammonia solution (7.2 g) were mixed in a sealed vessel and the solution was shaken for 15 s at room temperature. To which solution was added tetraethoxysilane (TEOS) 1840 μL, and then the mixture was shaken for 15 s. The mixture was aged at room temperature for 20 h. The obtained silica and epoxyresin were added to a beaker in air, and stirred strongly at 145 °C until a gel was formed. After cooling down to room temperature naturally, the resulted gel were transferred into an alumina crucible with cover. After calcination at 750 °C for 1 h in air in a furnace, the SiO_x/C NPs were obtained as black powders. RGO network was prepared from purified natural graphite according to Hummers method as previous reports.[33, 34] The SiO_x/C@RGO NCPs was prepared through dispersing the two materials in ethanol solution. Firstly, 10 mg of RGO was ultrasonicated with 20 ml of ethanol for 1h. Secondly, 40 mg of the prepared SiO_x/C NPs powder was added into the solution under magnetic stirring for 2h to obtain a homogeneous suspension, then slowly drying at 50°C. During the solvent vaporization, the SiO_x/C NPs deposited gradually and embedded into the RGO network. The resultant solid products were collected by filtration and dried in vacuum at 80 °C for 12 h.

Physical characterization

Fourier transform infrared (FT-IR) spectroscopic measurements were made with an IR spectrophotometer (Brucker-Tensor 27, Germany) having a diffuse reflectance attachment ranging from 400 to 4000 cm^{-1} range. XRD analyses were performed on Rigaku D/MAX-RC X-ray diffractometer with Cu Ka 1 (45 kV and 50 mA). XPS analysis was performed on an ESCALab220i-XL electron spectrometer from VG Scientific using Al Ka line as the excitation source to evaluate the elemental compositions and chemical status of the samples. Raman spectrum was acquired on a Jobin Yvon HR800 confocal Raman system with 632.81nm diode laser excitation. FESEM analysis was performed on a Hitachi S-4700 equipped with EDAX. TEM and HRTEM analyses were performed on a JEM-2100F microscope with an accelerating voltage at 200kV. The electrical conductivities of the composites were measured at room temperature using a four-probe conductivity test metre (SB120; San Feng). Carbon element was analyzed using vario EL cube (Elementar, Germany). The specific surface area of the samples was determined by the gas sorption technique using a Micromeritics ASAP 2020 surface area analyzer based on the Brunauer-Emmett-Teller (BET) method.

Electrochemical Characterization

Electrochemical properties of the products were measured using CR2016 coin-type half-cells. The working electrodes were prepared by casting the slurry consisting of 80% active material, 10% sodium carboxymethyl cellulose (CMC), and 10% acetylene black onto a copper foil. Test cells were assembled in an argon-filled glove box with the metallic lithium foil as both the reference and counter electrodes, 1 M $LiPF_6$ in ethylene carbonate (EC)/dimethyl carbonate (DMC) (1:1 in volume) as the electrolyte, and a polypropylene (PP) micro-porous film (Cellgard 2300) as the separator. The cells were galvanostatically charged and discharged under different current densities over a voltage range of 0.01-1.5V on a Neware battery tester at room temperature. Cyclic voltammetry curves were measured at a scanning rate of 0.1 mV s^{-1} within the potential range of 0.01–3.0 V vs. Li/Li^+ using an electrochemistry working station (CHI660). The electrochemical impedance spectroscopy (EIS) test was carried out in the frequency range from 100 kHz to 10 mHz on an electrochemical workstation (CHI660). The weight of SiO_x/C@RGO NCPs in the working electrode was used to estimate the specific discharge capacity of the battery, which was expressed in mA hg^{-1} of SiO_x/C@RGO. On the basis of the equation described below, we could calculate a theoretical capacity (Q) of the hypothetical mixture of SiO_x/C@RGO, as follows:

$Q_{theoretical}=Q_{SiOx}\times$mass percentage of $SiO_x+Q_{Graphite}\times$mass percentage of Graphite $=2400\times64.08\% + 372\times35.92\% = 1671$ mA hg^{-1}

(The theoretical capacity of SiO_x was calculated on the basis of theoretical capacity of SiO previously reported.[48])

Results and discussion

Characterizations

The X-Ray diffraction (XRD, Fig. 1) patterns indicate that the SiO_x/C would consist of carbon (43°) and amorphous silicon oxide (SiO_2) (22°) with dispersed Si phase. The weak peaks of 28.4°, 47.3° and 56.1° are consistent with the standard values of Si (JCPDS no.27-1402). The breadth of the Si peaks suggests that Si crystal held in the NPs would have low crystallinity or be extremely small in size. The Fourier transform infrared (FT-IR) spectrum (Fig. 2a) reveals the coexistence of SiO_x, carbon, and RGO in the SiO_x/C@RGO. The spectrum shows a main peak at 1081cm^{-1} in both of SiO_x/C and SiO_x/C@RGO, which is assigned to the vibrational stretch of Si–O–Si belonging to SiO_x. The peak around 1606 cm^{-1} is assignable to C=C bond.[35] In Fig. 2b, the X-ray photoelectron spectroscopy (XPS) result demonstrats three dominative elements corresponded to C (C1s), Si (Si 2p and Si 2s), O (O1s).[36] Typical Si 2p spectra are shown in Fig. 2c, the spectra in the range of 98-106 eV are attributed to Si^0, Si^+, Si^{2+}, Si^{3+} and Si^{4+} from the low energy side, and the ratio of the valence state of Si was estimated from the area ratio of these spectra (Tab. 1). The average valence state of Si on the SiO_x/C is 2.04 and the Si/O atomic ratio was about 1.0. Energy dispersive X-ray analysis (EDAX) (Fig. S1†)

verifies the existence of element Si and O with approximately 1:1 ratio. In the Raman spectrum of SiO_x/C@RGO (Fig. 2d), a broad peak at 480 cm^{-1} extending asymmetrically down to approximate 430-515 cm^{-1} evidences the formation of amorphous SiO_x.[37] A sharp peak at 519 cm^{-1} is corresponding to Si crystal.[38] The two characteristic peaks at 1357 cm^{-1} and 1606 cm^{-1} are in good agreement with the typical Raman mode of D band and G band of RGO.[39] The result of carbon content analysis was confirmed that the residual carbon of SiO_x/C and SiO_x/C@RGO were 20.1 wt.% and 35.92 wt.% respectively, suggesting amorphous C and RGO in SiO_x/C@RGO was about 16% and 20 wt.% respectively.

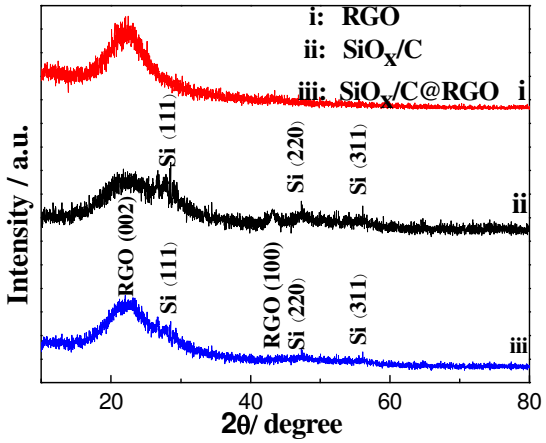

Fig.1 XRD patterns of RGO, SiO_x/C and SiO_x/C@RGO.

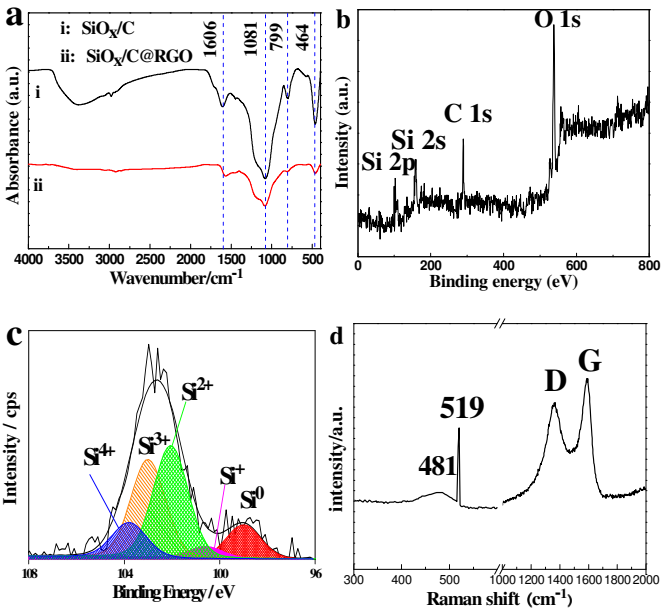

Fig.2 (a) FT-IR spectra of SiO_x/C and SiO_x/C@RGO, (b) XPS survey scan of SiO_x/C, (c) High-resolution XPS spectra of Si 2p for the SiO_x/C NPs sample and (d) Raman spectra of SiO_x/C@RGO with an excitation laser wavelength of 514.5 nm.

Tab. 1 Abundance ratios for Si oxidation states of Si 2p spectra with SiO_x/C NPs.

Sample	Si^0(%)	Si^+(%)	Si^{2+}(%)	Si^{3+}(%)	Si^{4+}(%)
SiO_x/C	11.8	3.97	40.63	32	11.6

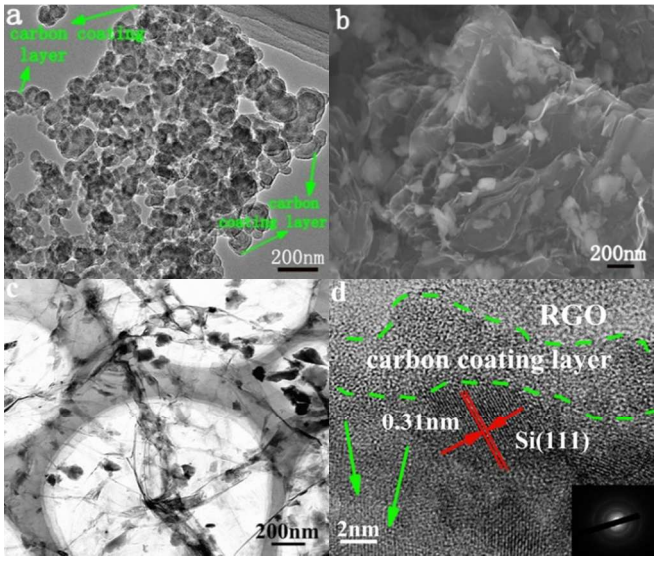

Fig. 3 (a) TEM image of SiO_x/C; (b) Top-view FESEM image of SiO_x/C@RGO; (c) TEM image of SiO_x/C@RGO; (d) HRTEM image and SAED pattern (inset) of SiO_x/C@RGO.

The size and morphology of the samples were characterized by field emission-scanning electron microscope (FESEM), transmission electron microscopy (TEM) and high-resolution TEM (HRTEM). From the TEM image of SiO_x/C (Fig. 3a), the primary SiO_x/C NPs coated by carbon layer (about 3nm thickness) display quasi-spherical shape with diameters of 50~100 nm in agreement with the FE-SEM image (Fig. S2†). It also shows that the SiO_x/C NPs are agglomerated. From the top-view (Fig. 3b) and cross-section view (Fig. 4a) FESEM images of SiO_x/C@RGO, we could observe the insertion of SiO_x/C NPs between the interlayers of RGO and the nanoporous composites with large amount of cavities were formed. The disorderly stacked layer by layer structure of the SiO_x/C@RGO also can be observed, which showed the feature of a 3D NCPs. The TEM image of SiO_x/C@RGO (Fig.3c) revealed that the carbon-coated SiO_x NPs are homogenously adhered to the surface of RGO, wrapped by RGO film or embedded in RGO network. Thus, a more effective 3D "sheet-web" mode mixed (electron and ion) conductive network [40-43] will be built around the active NPs, which also can enhance the electronic conductivity of active material and decrease the effect of particle-agglomeration phenomenon effectively in comparison with the RGO-free SiO_x/C NPs. The HRTEM image of the SiO_x/C@RGO NCPs (Fig. 3d) demonstrats that the SiO_x/C NPs in the final products are covered with a thin layer of amorphous carbon (3-5nm), and embedded into the RGO network. Lattice fringes were clearly displayed, and the d-spacing was derived to be 0.31 nm, corresponding to the spacing between (111) planes of Si crystal. In another HRTEM image of the SiO_x/C@RGO NCPs (Fig. S3†), crystalline planes of SiO_2 (210) with a distance spacing of 0.374 nm can also be clearly observed. The selected-area electron diffraction (SAED) pattern (Fig. 3d inset) comprised a well-resolved set of concentric rings with bright spots, indicating the nanocrystalline nature of the Si domain in SiO_x microstructure. The disordered domain (indicated by green arrows) in the NCPs should be amorphous SiO_x ($0 \le x \le 2$) microstructure. According to the XRD, RAMAN and HRTEM investigations, the SiO_x/C NPs structure could be described as a mixture of Si crystal, SiO_2 crystal and

amorphous SiO_x ($0 \le x \le 2$) microstructure. According to Brunauer-Emmett-Teller (BET) analysis, the specific surface area of SiO_x/C@RGO is 390.2 m^2 g^{-1} (Fig. S4†). The isothermal sorption profile suggested that the material contains mesopores with Barret-Joyner-Halenda (BJH) pore diameter of about 12.1 nm, which are the voids between aggregated NPs. Such a high surface area and typical mesoporous structure, in association with the co-modified strategy (carbon coating layer and ultrathin RGO network), must result in somewhat beneficial electrochemical effects of anode material in LIBs.[44,45]

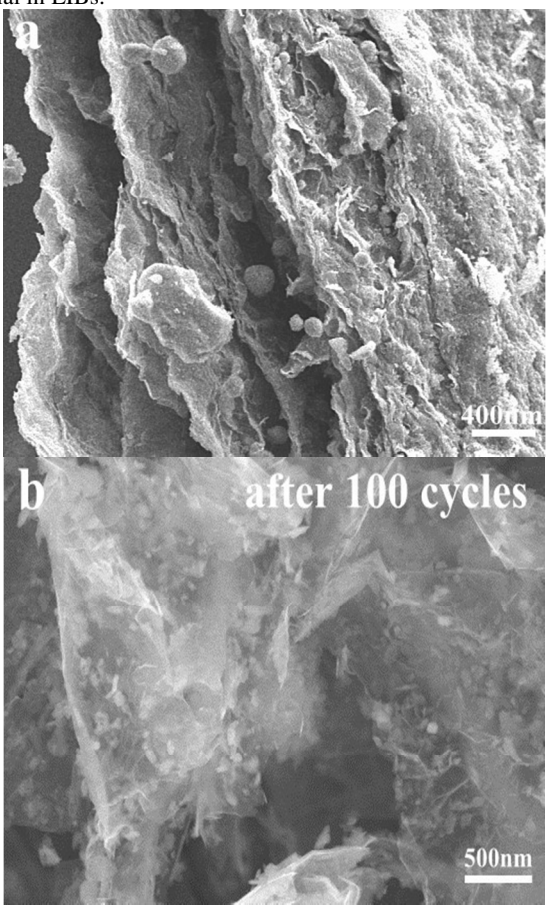

Fig. 4 (a) Cross-section view FESEM image of SiO_x/C@RGO NCPs, (b) FESEM image of SiO_x/C@RGO after 100 cycles under a current density of 100 mA g^{-1}.

The electrochemical performance of the SiO_x/C@RGO material as an anode for LIBs was tested using CR2016 coin-type half-cells. The discharge–charge profiles of electrodes during the 1st, 5th, 20th, 50th, 100th and 400th cycles at 100 mA g^{-1} between 0.01V and 1.5V are shown in Fig. 5a. The discharge–charge curves remain similar in shape, with a small decrease in the capacity from the 5th cycle to the 400th cycle. The initial irreversible capacity could be attributed to the formation of SEI film on the surface of the electrode. Fig. 6a shows the initial discharge and charge curves of various anodes. Specifically, SiO_x/C@RGO anode delivers a capacity of 2402.9 mAh g^{-1} in the first discharge and 1225.5 mAh g^{-1} in the first charge process, while SiO_x/C gives 2271.9 and 1053.9 mAh g^{-1} in the first discharge and charge process, respectively. These values of SiO_x/C@RGO were larger than that of SiO_x/C, which may be attributed to enhanced surface area (additional storage of Li-ions in the defects) or stacking of nanoscale composites. The initial coulombic efficiencies were 51% and 46.39% for SiO_x/C@RGO and SiO_x/C respectively. Compared to SiO_x/C, the lower irreversible capacity loss of SiO_x/C@RGO can be attributed to the less formation of the SEI layer and the side reaction of the electrolyte.[50] Due to the coexistence of carbon coating layer and RGO, direct contact between SiO_x core and electrolyte was avoided to a great extent, prohibiting the formation of SEI films on the SiO_x surface.

Pristine SiO_x/C NPs without RGO were also tested for comparison. As shown in Fig. 5b, the SiO_x/C@RGO NCPs exhibit a higher specific capacity and better cycling stability than the SiO_x/C NPs. After 100 cycles under a current density of 100 mA g^{-1}, the SiO_x/C@RGO NCPs still retain a reversible capacity of 1284 mAh g^{-1}, which is 3 times higher than the theoretical capacity of graphite, whereas the SiO_x/C NPs only show a specific capacity of 757.9 mAh g^{-1}. The reversible capacity of SiO_x/C@RGO NCPs after 400 cycles is observed to be 1264 mAh g^{-1}, which is 84.3% of the discharge capacity in the 5th cycle (Fig. S5†). It is noteworthy that the Coulombic efficiency is always above 98% since the 4th cycle and keeps a stable trend in the process of recharging even after 400 cycles.

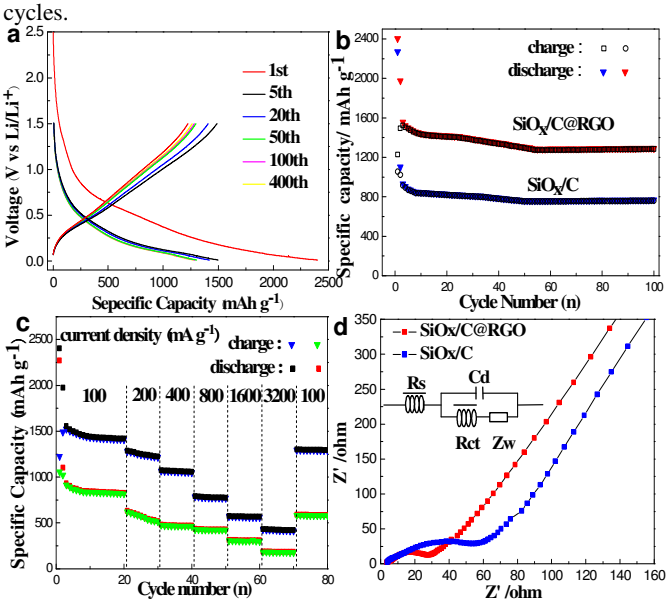

Fig. 5 (a) Discharge-charge curves of SiO_x/C@RGO cycled between 0 and 1.5 V under a current density of 100 mA g^{-1} for the 1st, 5th, 20th, 50th and 100th and 400th cycle; (b) Cycling behaviors of SiO_x/C@RGO and SiO_x/C under a current density of 100 mA g^{-1}; (c) Cycling performances of SiO_x/C@RGO and SiO_x/C under different current densities; (d) Nyquist plots of the electrodes of SiO_x/C@RGO and SiO_x/C.

The rate performance of SiO_x/C@RGO NCPs anode was also tested at current densities of 100 mA g^{-1}, 200 mA g^{-1}, 400 mA g^{-1}, 800 mA g^{-1}, 1600 mA g^{-1} and 3200 mA g^{-1} in comparison with SiO_x/C NPs. As shown in Fig. 5c, the charge capacity of SiO_x/C@RGO NCPs at the current density of 800 mA g^{-1} was 770mAh g^{-1}; even under the very high current density of 3200 mA g^{-1}, it retains a high capacity of 412.3 mAh g^{-1}. While the charge capacity of SiO_x/C NPs is 420.8 and 176.2 mAh g^{-1} at the current density of 800mA g^{-1} and 3200 mA g^{-1}, respectively. After the current density returned to 100 mA g^{-1}, the SiO_x/C@RGO NCPs delivered a capacity of about 1286.4 mAh g^{-1}, showing that the electrode was not damaged by the high rate test. Fig. 6b shows the Cyclic voltammograms (CV) profiles of the as-prepared SiO_x/C@RGO NCPs. In the cathodic polarization process

of the first cycle, the cathodic peak around 0.75 V (vs. Li/Li^+) could be ascribed to the formation of SEI layers on the surface of active materials, the reduction of SiO_2 to Si and the synchronous formation of Li_2O and Li_4SiO_4 [11, 13], as described in Eq. (1) and Eq. (2):

$$2SiO_2+4Li \rightarrow Li_4SiO_4+Si \quad (1)$$

$$SiO_2+4Li \rightarrow 2Li_2O+Si \quad (2)$$

The cathodic peak at about 0.02 V corresponds to alloying of Si with Li and the reversible reaction between Li and carbon (including carbon coating layer and RGO network)[27, 49], as described in Eqs.(3) and (4) respectively:

$$Si+xLi \leftrightarrow Li_xSi \quad (0 \le x \le 4.4) \quad (3)$$

$$2C+Li \leftrightarrow LiC_2 \quad (4)$$

In the anodic polarization process of the first cycle, the anodic peak at 0.50 V could be ascribed to dealloying of Li-Si alloys, as described in Eq. (5):

$$Li_xSi \leftrightarrow Si+xLi \quad (0 \le x \le 4.4) \quad (5)$$

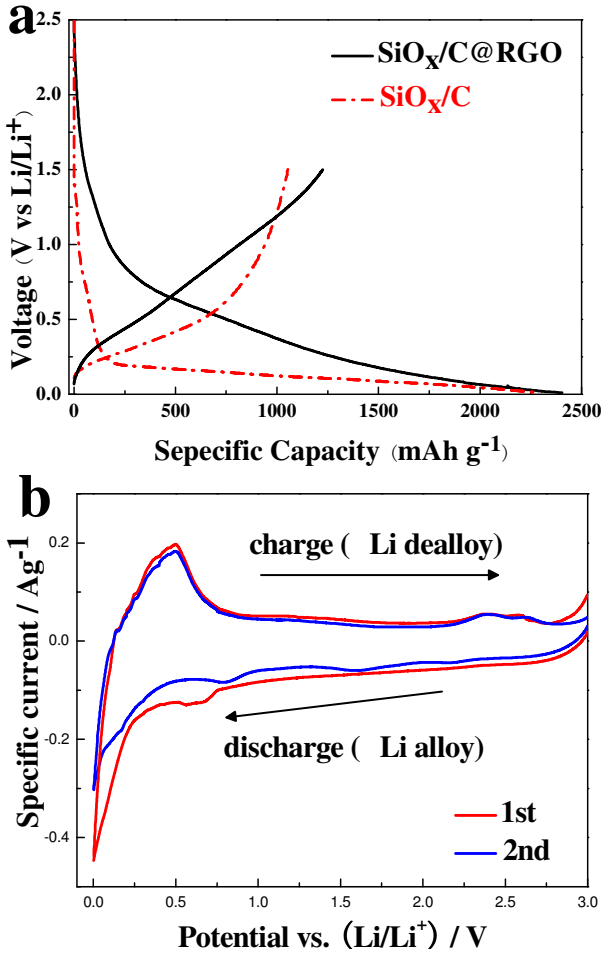

Fig. 6 (a) The first charge-discharge voltage curves of SiO_x/C@RGO and SiO_x/C at constant current of 100 mA g^{-1}, (b) The CV curves of the as-prepared SiO_x/C@RGO NCPs measured in the voltage range of 0.01-3.0 V with a scan rate of 0.1 mV s^{-1}.

Electrochemical impedance spectroscopy (EIS) measurements were carried out to investigate the effect of incorporation of RGO. Fig. 5d shows the Nyquist plots of the SiO_x/C@RGO NCPs and SiO_x/C NPs electrode. The SiO_x/C@RGO NCPs electrode shows a much lower charge transfer resistance (Rct) than does the SiO_x/C electrode (27.2 vs 53.7 Ω) on the basis of the modified Randles equivalent circuit given in the inset of Fig. 5d, which is consistent with the results of the four-probe conductivity measurement. The electric conductivities of SiO_x/C@RGO NCPs and SiO_x/C NPs are 1.26×10^{-3} S·cm^{-1} and 8.79×10^{-4} S·cm^{-1}, respectively. The robust structure of the SiO_x/C@RGO NCPs is confirmed by the FESEM image of the sample after being used in LIBs for 100 cycles (Fig. 4b). As shown in the image, SiO_x/C NPs remain integrated with RGO network after 100 cycles at 100 mA g^{-1}, showing that the electrode was not damaged by the cycling test. These results indicate that the incorporation of RGO had improved the electronic conductivity, and thus improved the rate capability and reversible capacity compared to the RGO-free SiO_x/C NPs. The superior electrochemistry performance of SiO_x/C@RGO NCPs can be attributed to the synergistic effect between carbon coating layer and RGO network as follows: (1) the carbon coating layer functions as a stabilizer to immobilize SiO_x NPs, a matrix to buffer local volume changes during cycling, and a conducting bridge between RGO and SiO_x NPs. Therefore mechanical stability and electrical contact were increased for SiO_x/C@RGO NCPs; (2) due to its distinctive properties, RGO network which is tough and elastic enough to compensate the large volume change of the SiO_x NPs, prevent the aggregation of SiO_x/C NPs, and maintain a high electrical conductivity of the overall electrode, thus realizing much improved specific capacity, cycling performance, and rate capability as an anode material for LIBs.

Conclusions

In summary, a facile approach for the preparation of 3D SiO_x/C@RGO NCPs was synthesized as an anode for LIBs. By a comparative study on the electrochemical performance of SiO_x/C@RGO and SiO_x/C, we have demonstrated that the specific capacity, rate capability and cycling stability are significantly improved due to the addition of RGO material. These superior performances of the SiO_x/C@RGO in LIBs are due to the co-modification of carbon coating layer and RGO network effectively constructed a 3D conducting network through a "sheet-web" mode and thus enhanced the electrochemical activity of SiO_x/C effectively. This co-modification strategy provides a simple and feasible platform for further advances in high-capacity anode materials with large volume variations and low electrical conductivities in the field of storage energy devices.

Acknowledgement

We appreciate the support of National Natural Science Foundation of China (No. 50974045)

Notes and references

School of Chemical Engineering and Technology, Harbin Institute of Technology, Harbin, China. Fax: +86 451 86413721; Tel: +86 45186413751; E-mail: wangdianlonghit@163.com

† Electronic Supplementary Information (ESI) available: [details of any supplementary information available should be included here]. See DOI: 10.1039/b000000x/

1 B. Wang, J. S. Chen, *J. Am. Chem. Soc*, 2011, 133, 17146

2 Armand, M, Tarascon, J. M, *Nature*, 2008, 451, 652.

3 J. Yang, Y. Takeda and N. Imanishi, *Solid State Ionics,* 2002, 152, 125.

4 M. Miyachi, H. Yamamoto, *J. Electrochem. Soc*, 2005, 152, A2089.

5 Y. Nagao, H. Sakaguchi and H. Honda, *J. Electrochem. Soc*, 2004, 151, A1572.
6 L. Y. Beaulieu, K. W. Eberman and R. L. Turner, *Electrochem. Solid-State Lett*, 2001, 4, A137.
7 M. Yoshio, H. Wang. *J. Electrochem. Soc*, 2002, 149, A1598
8 Beattie, S. D, Larcher, D and Morcrette, *J. Electrochem. Soc*, 2008, 155, A158.
9 Mariko Miyachi, Hironori Yamamoto and Hidemasa Kawai, *J. Electrochem. Soc,* 2007, 1544, A376.
10 Toru Tabuchi, Hideo Yasuda and Masanori Yamachi, *J Power Sources,* 2005, 146, 507.
11 Q. Si, K. Hanai and T. Ichikawa, *J Power Sources,* 2011, 196, 9774.
12 Chil-Hoon Doh, Chul-Wan Park and Hye-Min Shin, *J Power Sources,* 2008, 179, 367.
13 Jing Wang, Hailei Zhao and Jianchao He*, J Power Sources,* 2001, 196, 4811.
14 Xianxia Yuan, Ya-Jun Chao and Zi-Feng Ma, *Electrochem commun,* 2007, 9, 2591.
15 Il Won Seong, Ki Tae Kim and Woo Young Yoon, *J Power Sources,* 2009, 189, 511.
16 Il Won Seong, Woo Young Yoon, *J Power Sources*, 2010, 195, 6143.
17 T. Zhang, J. Gao and H.P. Zhang, *Electrochem commun,* 2007, 9, 886.
18 Shinichi Komaba, Keiji Shimomura and Naoaki Yabuuchi, *J. Phys. Chem. C*, 2011, 115, 13487.
19 A. Guerfi, P. Charest and M. Dontigny, *J Power Sources*, 2011, 196, 5667.
20 Dale A.C. Brownson, Dimitrios K. Kampouris and Craig E. Banks, *J Power Sources*, 2011, 196, 4873.
21 Na Li, Minhua Cao and Changwen Hu, *Nanoscale*, 2012, 4, 6205.
22 Virendra Singh, Daeha Joung and Lei Zhai, *Prog Mater Sci,* 2001, 56, 1178.
23 Seung-Min Paek, EunJoo Yoo and Itaru Honma, *Nano Lett*, 2009, 9, 1.
24 Yu-Shi He, Da-Wei Bai and Xiaowei Yang, *Electrochem commun*, 2010, 12, 570.
25 Shu-Lei Chou, Jia-Zhao Wang and Mohammad Choucair, *Electrochem commun*, 2010, 12, 303.
26 Y.J. Mai, X.L. Wang and J.Y. Xiang, *Electrochimica Acta,* 2011, 56, 2306.
27 Peichao Lian, Xuefeng Zhu and Hongfa Xiang, *Electrochimica Acta,* 2010, 56, 834.
28 Haegyeom Kim, Dong-Hwa Seo and Sung-Wook Kim, *Carbon*, 2011, 49, 326.
29 Chenfeng Guo, Dianlong Wang and Qiuming Wang, *Int. J. Electrochem. Sci.*, 2012, 7, 8745.
30 Morishita T, Hirabayashi T and Okuni T, *J Power Sources,* 2006, 160(1), 638.
31 Zhang W-M, Hu J-S and Guo Y-G, *Adv Mater*, 2008, 20(6), 1160.
32 Robert I. Nooney, Dhanasekaran Thirunavukkarasu. *Chem. Mater,* 2002, 14, 4721.
33 Z. S. Wu, W. C. Ren and L. B. Gao, *Carbon*, 2009, 47, 493.
34 L. Wang and D. L. Wang, *Electrochim. Acta*, 2011, 56, 5010.
35 Douglas B. Mawhinney, John A. Glass and Jr., *J. Phys. Chem. B,* 1997, 101, 1202.
36 Mariko Miyachi, Hironori Yamamoto and Hidemasa Kawai, *J. Electrochem. Soc,* 2005, 152(10), A2089.
37 D. Nesheva, C. Raptis and A. Perakis, *J. Appl. Phys,* 2002, 92, 4678.
38 N. Wang, Y.H. Tang and Y.F. Zhang, *Chem Phys Lett,* 1999, 299, 237.
39 I. Francis Cheng, Yuqun Xie, *Carbon,* 2011, 49, 2852.
40 C. Su, X. D. Bu and L. H. Xu, *Electrochim. Acta*, 2012, 50, 64, 190.
41 L. Wang, H. B. Wang and Z. H. Liu, *Solid State Ionics,* 2010, 181, 1685.
42 X. F. Zhou, F Wang and Y. M. Zhu, *J. Mater. Chem.*, 2011, 5521, 3353.
43 Y. Wang, Z. S. Feng, J. J. Chen and C. Zhang, *Mater. Lett.*, 2012, 71 , 54.
44 Z. S. Wu, W. C. Ren and L.Wen, *ACS Nano,* 2010, 4, 3187.
45 C. X. Guo, H. B. Yang and Z. M. Sheng, *Angew. Chem., Int. Ed.*, 2010, 49, 3014.
48 Jae-Hun Kim, Cheol-Min Park and Hansu Kim, *J. Electroanal Chem,* 2011. 08. 010.
49 X. Wang, X. Zhou and K. Yao, *Carbon*, 2011, 49, 133.
50 T. Nakajima, V. Gupta and Y. Ohzawa, *J Power Sources*, 2004, 137, 80.

